Highlights

Physics-informed multiscale modelling of tunnelling-governed percolation and conductivity evolution in carbon black modified cementitious composites

Jeslin Thalapil, Ye Lu

- Introduces a physics-informed tunnelling framework for predictive modelling of conductive transport in self-sensing cementitious nanocomposites.
- Explicitly captures distance-dependent quantum tunnelling through multilayer discretized interphase conductivity evolution.
- Quantifies the influence of tunnelling interaction distance on percolation transition and conductive network stability.
- Accurately predicts the experimentally observed conductivity transition near the percolation threshold in carbon black modified cementitious composites.
- Establishes a computationally efficient multiscale methodology for the design and optimization of self-sensing cementitious materials.

Physics-informed multiscale modelling of tunnelling-governed percolation and conductivity evolution in carbon black modified cementitious composites

Jeslin Thalapil[a], Ye Lu[a*]

[a] *Department of Civil & Environmental Engineering, Monash University, Clayton 3168, VIC, Australia*

Abstract

Self-sensing cementitious composites (SSCCs) containing conductive nanofillers enable structural health monitoring through measurable electrical responses. However, conventional numerical models generally assume homogeneous interphase conductivity, neglecting the distance-dependent quantum tunnelling that governs conductive network formation near the percolation threshold. This study presents a physics-informed multiscale framework for predicting the effective electrical conductivity (EEC) and percolation threshold (PT) of carbon black nanoparticle (CBN) modified cementitious composites. Stochastic representative volume elements were coupled with finite element simulations, while the tunnelling region surrounding each particle was discretized into concentric layers with exponentially decaying conductivity derived from Simmons' tunnelling theory. The framework reproduced the experimentally observed percolation threshold near 2 wt.% CBN and captured the conductivity increase from approximately 10^{-6} to 10^{-1} S/m. Compared with the homogeneous interphase model, the discretized tunnelling formulation substantially improved prediction accuracy, with the ten-layer model reducing the logarithmic root mean square error (RMSE) from 0.520 to 0.132. The proposed framework provides a physically realistic and computationally efficient approach for modelling tunnelling-mediated transport and optimizing self-sensing cementitious composites.

* Corresponding Author
Email: ye.lu@monash.edu

Keywords: Self-sensing cementitious composites; Quantum tunnelling; Percolation threshold; Carbon black nanoparticles; Multiscale finite element modelling; Tunnelling-mediated conductivity.

---

1. Introduction

Self-sensing cementitious composites (SSCCs) incorporating conductive nanofillers have attracted significant attention for distributed structural health monitoring due to their ability to transduce mechanical deformation into measurable electrical responses through piezoresistive mechanisms [1–4]. Unlike externally attached sensing systems, SSCCs intrinsically integrate sensing functionality within the cementitious matrix, enabling continuous monitoring without compromising structural compatibility or durability [5,6]. Electrical transport in these composites is governed by the formation and evolution of conductive pathways between dispersed conductive fillers, where conductivity increases sharply once the filler concentration exceeds the percolation threshold (PT) [7]. Near the PT region, electrical conduction is dominated not only by direct particle-to-particle contact, but also by quantum tunnelling across nanoscale interparticle gaps, rendering tunnelling-mediated transport fundamental to the electromechanical behaviour of conductive cementitious materials [8,9].

Among various conductive fillers investigated for SSCCs, including carbon nanotubes (CNTs), graphene nanoplatelets, and carbon fibers, carbon black nanoparticles (CBNs) offer a cost-effective alternative due to their high intrinsic conductivity, commercial availability, and scalability for large-volume cementitious applications [10–12]. Despite their relatively low aspect ratio compared with CNT-based systems, CBN-modified composites exhibit pronounced conductivity enhancement near the PT, indicating that tunnelling-assisted conduction plays a dominant role in conductive network formation [13]. The overall conductive response of the heterogeneous composite is commonly represented by its effective electrical conductivity (EEC), which reflects the resultant bulk conductivity arising from the stochastic spatial distribution of conductive particles,

interparticle tunnelling interactions, and conductive pathway connectivity within the representative volume element (RVE). The electrical behaviour of these systems is strongly governed by filler concentration, interparticle spacing, dispersion quality, and interfacial interactions between conductive particles and the cementitious matrix [14]. Consequently, accurate prediction of PT and EEC remains a critical challenge in the design and optimization of SSCCs for sensing applications.

Experimental investigations have demonstrated that the electrical behaviour of conductive cementitious composites is strongly influenced by conductive filler concentration, particle dispersion, interfacial conductivity, pore structure, and conductive pathway connectivity [15–19]. However, experimental characterization of conductive transport evolution near the PT is often resource-intensive due to the coupled influence of microstructural heterogeneity and stochastic conductive pathway formation. Consequently, analytical and numerical modelling approaches have increasingly been employed to investigate conductivity evolution and optimize conductive composite design.

Classical effective medium and percolation-based formulations, including Maxwell–Garnett, Bruggeman, and McLachlan-type models, have been widely used to estimate conductivity evolution in conductive composite systems [20–23]. Although these approaches provide useful macroscopic approximations, they rely primarily on homogenized assumptions that do not explicitly capture localized conductive pathway formation or nanoscale tunnelling interactions between neighbouring conductive particles.

To overcome these limitations, stochastic finite element and Monte Carlo-based RVE frameworks have increasingly been employed to explicitly model conductive network evolution within heterogeneous conductive composites [24–29]. Several studies have implemented hard-core/soft-shell formulations to represent conductive particles surrounded by electrically active tunnelling interaction regions [30–33]. In these approaches, conductive overlap between neighbouring soft-shell domains enables tunnelling-assisted conductive transport prior to direct particle contact.

Despite these advances, most existing numerical frameworks assume homogeneous conductivity throughout the electrically active interphase region. Such assumptions are physically inconsistent with Simmons-type quantum tunnelling behaviour, in which electron transmission probability decays exponentially with increasing interparticle separation distance [34]. Consequently, homogeneous interphase formulations often smooth conductivity evolution near the PT and fail to realistically reproduce the sharp conductivity transitions experimentally observed in conductive cementitious nanocomposites. Physically realistic prediction of conductive transport near the PT therefore requires explicit incorporation of spatially varying tunnelling conductivity within the interphase domain. Implementation of distance-dependent tunnelling conductivity within fully resolved three-dimensional (3D) conductive network simulations, however, introduces substantial computational complexity due to the large number of conductive interactions and geometric discretization requirements. Therefore, a computationally efficient and physically realistic modelling framework capable of explicitly incorporating tunnelling-mediated conductive transport remains necessary for predictive investigation of conductive cementitious composites.

To address these limitations, this study presents a physics-informed multiscale numerical framework for modelling tunnelling-governed conductivity evolution in carbon black nanoparticle modified SSCCs. A stochastic RVE framework coupled with electro-thermal finite element simulations was developed to explicitly capture conductive pathway evolution within heterogeneous cementitious microstructures. To realistically represent tunnelling-assisted conductive transport, the electrically active interphase surrounding conductive particles was discretized into concentric conductive layers with exponentially decaying conductivity derived from Simmons' quantum tunnelling theory. The novelty of this work lies in: (1) the development of a discretized tunnelling interphase framework incorporating Simmons-based conductivity decay; (2) implementation of a stochastic multiscale finite element methodology for modelling tunnelling-mediated conductive transport in CBN modified cementitious composites; (3) quantitative experimental

validation of conductivity evolution and percolation behaviour near the PT region; and (4) establishment of a computationally efficient predictive framework for investigating conductive pathway evolution in self-sensing cementitious materials.

2. Experimental program

2.1. Materials and mix design

Ordinary Portland cement (OPC) blended with 10 wt.% silica fume was used as the cementitious binder system. Commercially available VULCAN XC72® CBNs with an average particle diameter of approximately 30 nm were incorporated as conductive fillers. The physical characteristics of the CBN are summarized in Table 1 [35,36].

Table 1: Properties of Vulcan XC72R® CBN.

Property	Value
Diameter (nm)	20 to 50
Bulk conductivity $\left(\frac{S}{m}\right)$	277
Specific surface area $\left(\frac{m^2}{g}\right)$	250
Iodine number $\left(\frac{mg}{g}\right)$	253
325 mesh residues (ppm)	$\leq$ 10
Density $\left(\frac{kg}{m^3}\right)$	96

A polycarboxylate ether-based superplasticizer (Sika® ViscoCrete®-10) was added at 1 wt.% of binder content [37] to improve nanoparticle dispersion within the cementitious matrix. Deionized water was used throughout the specimen preparation process, with a water-to-binder ratio of 0.45 [38] adopted to balance workability and conductivity performance. CBN dosage was varied from 0 to 5 wt.% by binder weight to experimentally capture conductivity evolution across sub-percolation and post-percolation regimes. This concentration range was selected based on previous studies reporting

percolation transitions in carbon black modified cementitious systems within similar dosage intervals [39–41].

2.2. Specimen preparation

To minimize nanoparticle agglomeration and improve conductive filler dispersion within the cementitious matrix, the required quantity of CBN was initially dispersed in deionized water containing superplasticizer through mechanical stirring followed by ultrasonication at 20 kHz for 20 min [42]. The cementitious binder constituents were subsequently dry mixed prior to gradual addition of the conductive nanoparticle suspension under continuous mechanical mixing. Figure 1 illustrates the specimen preparation procedure and the progressive improvement in CBN dispersion achieved through combined superplasticizer treatment and ultrasonication. This procedure ensured stable CBN suspensions with substantially reduced agglomeration, thereby improving conductive filler dispersion within the cementitious matrix.

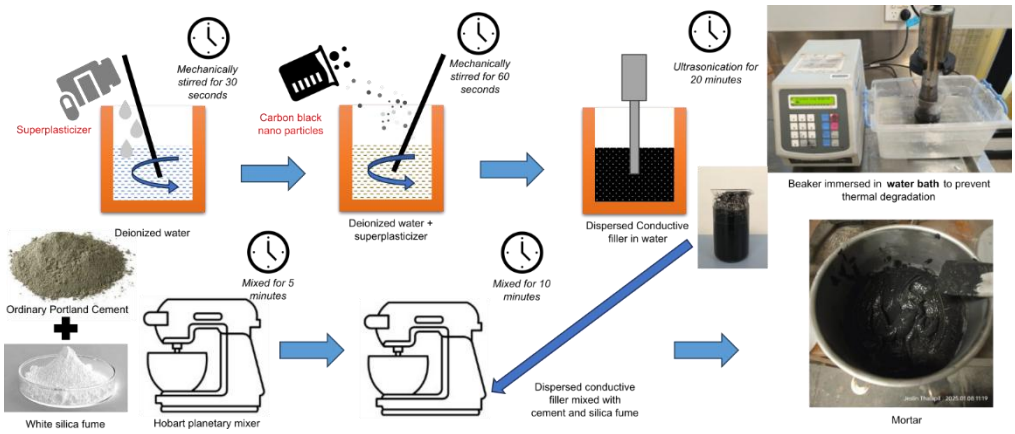

Figure 1:Schematic illustration of the preparation process for SSCC incorporating CBN.

The resulting cementitious composite mixture was cast into 50 mm cubic moulds in three layers with vibration-assisted compaction to minimize entrapped air voids and improve conductive filler distribution throughout the specimen volume. Specimens were demoulded after 24 h and cured under controlled laboratory conditions at 25°C and 95% relative humidity for 28 days.

Prior to electrical characterization, all specimens were oven dried at 60°C for 24 h to minimize moisture-induced conductivity variation and reduce ionic conduction contributions associated with pore solution transport.

2.3. Electrical conductivity measurement

Electrical resistance measurements were conducted using a two-probe direct current method with copper plate electrodes attached to opposite faces of the cubic specimens using silver conductive paste, as shown in Figure 2. Compared with embedded electrode configurations, the adopted surface-mounted arrangement minimizes stress-induced interfacial cracking while enabling bulk conductivity characterization of the composite. The two-probe approach was selected to capture the overall electrical response of the conductive network, including contributions from filler connectivity, interparticle tunnelling, and matrix-filler interfacial effects.

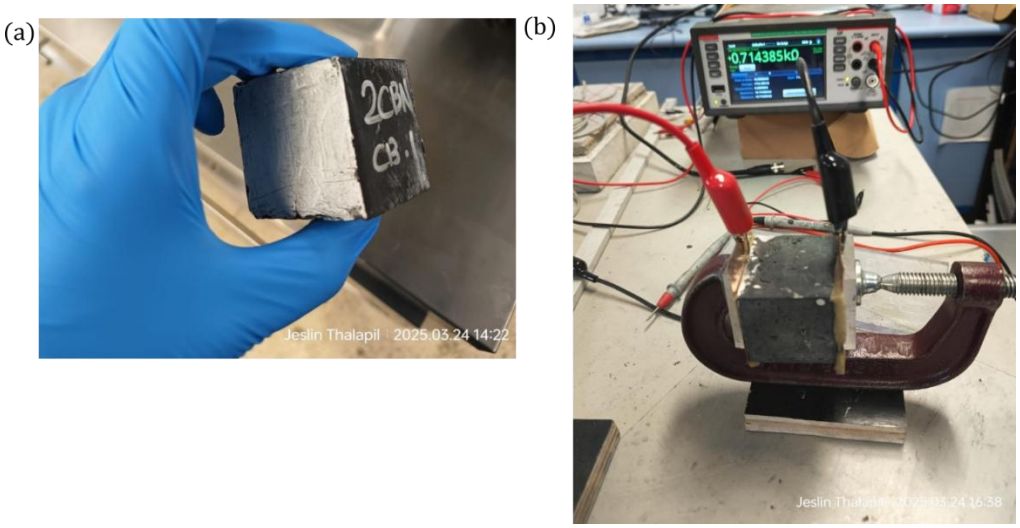

Figure 2: (a) Schematic illustration of silver conductive paste electrodes attached to opposing faces of a 50 mm SSCC cube modified with CBN (b) Experimental setup for resistance measurement of the SSCC using a Keithley DAQ6510 multimeter

A Keithley DAQ6510 digital multimeter was used to measure electrical resistance. The electrical resistivity, ρ, was calculated as $\rho = {}^{RA}/_{L}$,where R is the measured bulk resistance, A is the electrode cross-sectional area and L is the electrode spacing. The conductivity of the specimen is $\sigma_{eff} = {}^{1}/_{\rho}$.

Electrical conductivity measurements were performed for all CBN concentrations between 0 and 5 wt.%. For each composition, four independent specimens were tested and the reported conductivity values represent the mean response.

During direct current electrical measurements, transient electrode polarization effects were observed immediately following voltage application due to ionic accumulation at the electrode–matrix interface. It is understood that the conductivity measurements obtained prior to substantial polarization development were considered most representative of the intrinsic conductive network behaviour [43]. Consequently, the adopted measurement procedure primarily captures the bulk conductive behaviour associated with conductive pathway formation and tunnelling-mediated electron transport within the cementitious composite.

Figure 3 presents the experimentally measured conductivity evolution, demonstrating a pronounced conductivity increase between 2 and 3 wt.% CBN corresponding to the percolation transition region, which is consistent with the previous studies [44].

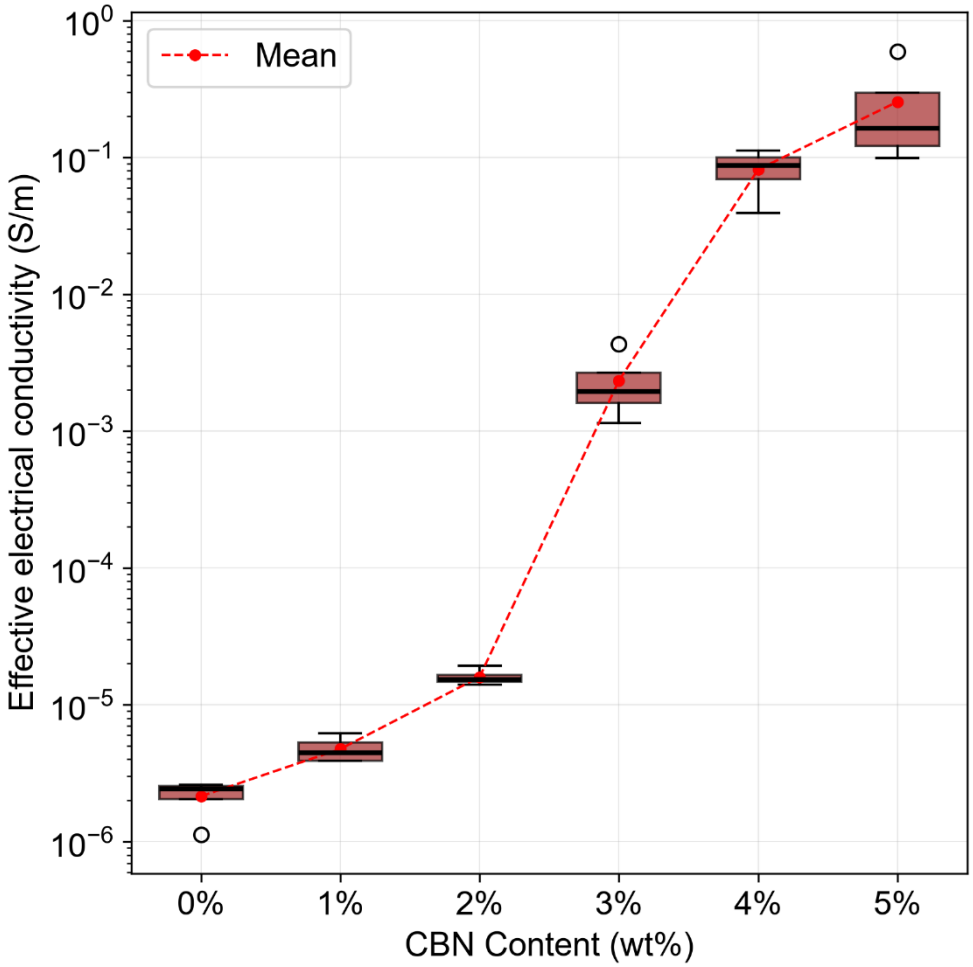

Figure 3: EEC of SSCCs as a function of CBN concentration. Reported values represent the average response of four independent specimens. A pronounced conductivity transition is observed near the percolation threshold between 2 and 3 wt.% CBN.

3. Physics-informed numerical framework

3.1. Tunnelling-mediated conductive transport

Electrical transport in conductive cementitious composites is governed by the formation and evolution of interconnected conductive pathways between dispersed conductive fillers embedded within the insulating cementitious matrix. At conductive filler concentrations below the PT, conductive particles remain largely isolated and the composite behaviour is dominated by the low intrinsic conductivity of the cementitious matrix. As conductive filler concentration increases, conductive pathways progressively emerge through a combination of direct particle contact and quantum tunnelling across nanoscale

interparticle separations. Near the PT region, tunnelling-mediated conductive transport becomes the dominant mechanism governing the sharp conductivity transition experimentally observed in conductive cementitious nanocomposites.

Classical effective medium [25] and percolation-based formulations provide useful macroscopic approximations of conductivity evolution but do not explicitly capture localized conductive pathway formation or nanoscale tunnelling interactions between neighbouring conductive particles. Consequently, physically realistic prediction of conductive transport near the PT requires direct microstructure-based numerical modelling capable of incorporating distance-dependent conductive interactions within heterogeneous conductive networks. Quantum tunnelling between adjacent conductive particles was modelled using Simmons' tunnelling formulation [45], in which tunnelling conductivity decays exponentially with increasing interparticle separation distance:

$$\sigma_t(d) = \sigma_0 e^{(-\beta d)} \quad (1)$$

where $\sigma_t(d)$ is the tunnelling conductivity at separation distance d, σ_0 is the electrical conductivity of the conductive particle and β is the tunnelling decay coefficient determined by the electron potential barrier characteristics. This exponential decay relationship governs conductive pathway evolution near the PT and forms the physical basis for the discretized interphase modelling framework developed in this study.

3.2. Multiscale RVE generation and finite element implementation

A multiscale RVE framework was developed to simulate conductive network evolution in CBN modified cementitious composites. To establish a direct correspondence between the numerical model and the experimental mixtures, the CBN content prescribed in each RVE was derived from the filler dosage

used during specimen preparation. The conductive filler volume fraction corresponding to each experimental CBN dosage was determined by converting filler weight fraction into an equivalent volume fraction using the densities of the conductive filler and cementitious matrix:

$$Vol\%_{CBN} = \frac{wt\%_{CBN}/\rho_{CBN}}{wt\%_{CBN}/\rho_{CBN} + wt\%_{matrix}/\rho_{matrix}} \quad (2)$$

where V_f is the conductive filler volume fraction, $wt\%_{CBN}$ and $wt\%_{matrix}$ are the filler and matrix weight fractions, respectively, and ρ_{CBN} is the density of CBN, and ρ_{matrix} is the density of OPC. The dry bulk densities of CBN and OPC were experimentally measured as 96 and $1440\ ^{kg}/_{m^3}$, respectively, using dry-powder measurement procedure. These values were consistent with corresponding dry bulk densities reported in the manufacturer specifications and literature [46] and were therefore used to calculate the equivalent apparent volume fractions adopted in the numerical model.

Assuming spherical conductive particles with average radius r, the volume of an individual conductive particle was calculated as $V_P = \frac{4}{3}\pi(r)^3$. The total number of conductive particles within the RVE domain was subsequently determined from:

$$N = \frac{Vol\%_{CBN} \times V_{RVE}}{V_P} \quad (3)$$

where N is the total number of conductive particles and V_{RVE} is the total RVE volume. Vulcan XC72R® CBNs with an average particle diameter of approximately 30 nm were adopted throughout the simulations. Table 2 summarizes the corresponding conductive filler volume fractions and particle populations used for the stochastic RVE generation framework.

Table 2: Estimated number of VULCAN XC 72R® CBN with a diameter of 30 nm contained within a 1000x1000x1000 nm³ 3D RVE cube at various weight percentages.

CBN weight fraction, $wt\%_{CBN}$	**Equivalent volume fraction, $Vol\%_{CBN}$**	**Number of particles, N**
0.0%	0.0%	0
1.0%	13.16%	9,308
2.0%	23.44%	16,579
3.0%	31.69%	22,417
4.0%	38.46%	27,206
5.0%	44.12%	31,207

All numerical simulations were performed on a high-performance workstation equipped with an Intel® Core™ i7-13700 processor operating at 2.10 GHz and 32 GB of RAM. Initially, fully resolved 3D conductive network models were generated using a Monte Carlo-based random sequential adsorption algorithm implemented within ABAQUS. Conductive particles were randomly distributed throughout the computational domain while enforcing a minimum centre-to-centre separation greater than or equal to twice the particle radius, thereby preventing geometric overlap:

$$\sqrt{(x_i - x_j)^2 + (y_i - y_j)^2 + (z_i - z_j)^2} \geq 2r \tag{4}$$

where (x_i, y_i, z_i) and (x_j, y_j, z_j) represent neighbouring conductive particle coordinates and r is the conductive particle radius. Representative 3D RVEs generated using the proposed stochastic framework are illustrated in Figure 4(a).

Although fully resolved 3D conductive network models provide a more realistic representation of particle connectivity, their computational requirements increase rapidly with conductive filler concentration due to the large number of particles, geometric interactions and finite element discretization requirements.

Preliminary 3D simulations demonstrated rapid increases in computational complexity with increasing conductive filler concentration, for instance, generating a 3D RVE with 0.25 wt% CBN (2,563 particles) required approximately eight hours.

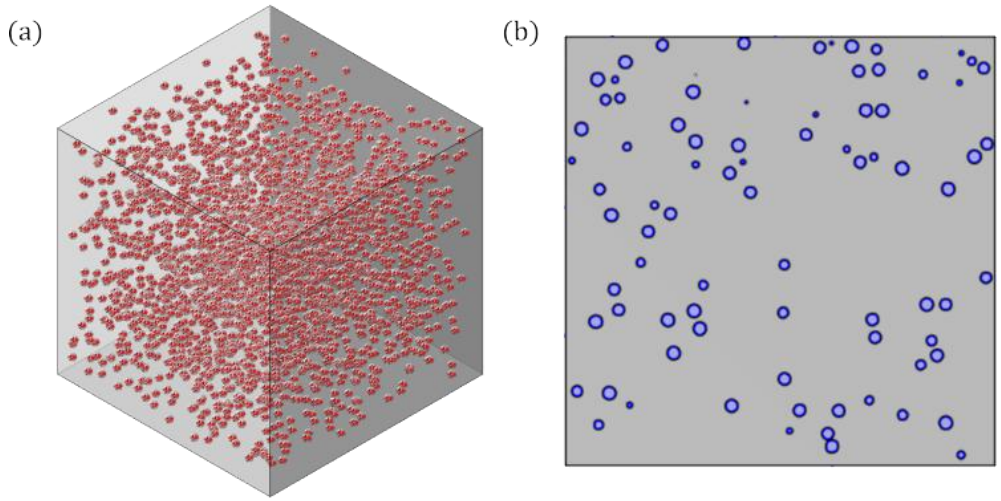

Figure 4: (a) 3D RVE illustrating the random spatial distribution of CBN within a cement matrix. The RVE (dimensions: 1000 × 1000 × 1000 nm) with 0.25 wt% of CBN of size 30 nm diameter (b) Cross-sectional 2D view showing the distribution of CBN particles in the RVE.

Consequently, a complementary two-dimensional (2D) stochastic RVE framework was adopted to enable computationally efficient parametric investigation while preserving the dominant nearest-neighbour percolation physics governing tunnelling-mediated conductive transport. Since percolation onset is governed primarily by local conductive connectivity statistics, the reduced-order 2D framework provides a computationally tractable approximation of conductive network evolution while significantly reducing simulation expense.

To ensure statistical representativeness of conductive pathway formation, the influence of RVE size on predicted EEC was evaluated by systematically varying the computational domain size from 100 to 1500 nm while maintaining constant conductive filler concentration. Figure 5 presents the variation in predicted conductivity and total computational time with increasing RVE size for the case containing 5 wt% CBN. The results demonstrate that predicted

conductivity stabilizes for RVE sizes approaching 1000 nm, indicating convergence toward statistically representative conductive network behaviour. Although larger RVEs further reduce stochastic variability, the associated computational cost increases substantially due to the rapid growth in conductive interactions and finite element complexity. Consequently, a 1000 nm RVE was adopted as an optimal balance between prediction accuracy and computational efficiency for subsequent simulations.

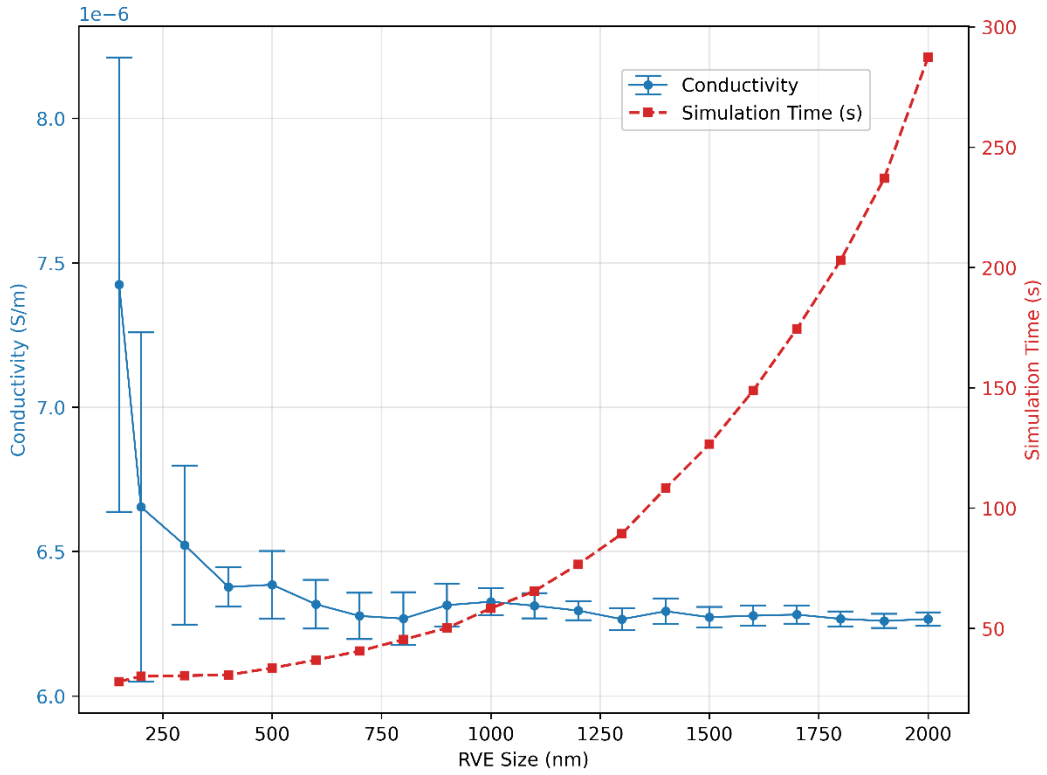

Figure 5: Variation of EEC (S/m) and total simulation time (s) with RVE size containing 5 wt% carbon black nanoparticles. The dual-axis plot illustrates the convergence of conductivity values for larger RVE sizes and the sharply increasing computational cost as domain size grows.

A mesh sensitivity analysis was subsequently conducted using the optimized 1000 nm RVE domain. Ten independent Monte Carlo realizations were analysed for mesh sizes ranging from 1 to 10 nm using coupled DC2D8E and DC2D6E electro-thermal elements. Figure 6 presents the variation in predicted conductivity and computational time with increasing mesh refinement. The results demonstrate that predicted conductivity remains relatively stable across

the investigated mesh range, indicating mesh-independent conductive transport behaviour. In contrast, computational time increased substantially with progressive mesh refinement due to the rapid increase in element count and conductive interaction resolution. Extremely fine meshes produced only marginal improvement in conductivity prediction while significantly increasing computational expense. Consequently, a mesh size of 5 nm was adopted for subsequent simulations.

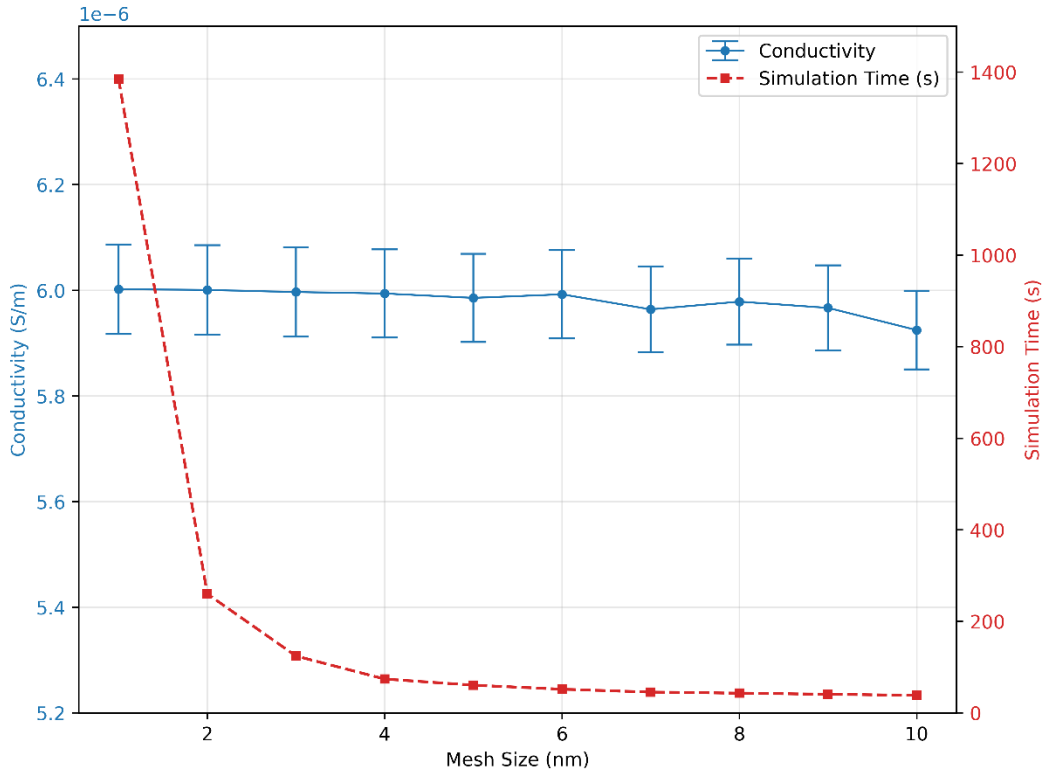

Figure 6: Influence of mesh size on predicted EEC and total simulation time for a 1000 nm RVE using DC2D8E + DC2D6E coupled electro-thermal elements. Conductivity predictions remain stable across the investigated mesh range, while computational time increases substantially with mesh refinement.

Table 3 shows the calculated number of particles inside the 2D square RVE of 1000 nm size for increasing weight percentages of VULCAN XC 72R CBN particles.

Table 3: CBN Particle distribution in 1000 nm 2D RVE with 30 nm CBN size.

CBN weight fraction, $wt\%_{CBN}$	**Equivalent area fraction, $Area\%_{CBN}$**	**Number of particles, N**

0.0%	0.0%	0
1.0%	13.16%	187
2.0%	23.44%	332
3.0%	31.69%	449
4.0%	38.46%	545
5.0%	44.12%	625

Finite element simulations were conducted using coupled electro-thermal analysis within ABAQUS/Standard. The cementitious matrix was assigned low intrinsic electrical conductivity, while conductive CBN particles were assigned conductivity corresponding to Vulcan XC72R® carbon black. Steady-state electrical conduction was simulated by applying electrical potential boundary conditions across opposing RVE boundaries. The resulting electrical current output was subsequently used to determine the EEC of the composite system. To ensure statistical reliability, ten independent Monte Carlo realizations were generated for each conductive filler concentration and tunnelling parameter combination. Preliminary statistical analyses demonstrated that ten realizations were sufficient to achieve convergence in the conductivity distribution and associated stochastic variability. Averaged conductivity values obtained from independent realizations were subsequently used to evaluate conductivity evolution and percolation behaviour. Compared with the fully resolved 3D framework, the computational efficiency of the reduced-order 2D approach was substantially improved. For example, generation of a 2D RVE containing 0.25 wt.% CBN (52 particles) required approximately 40 seconds.

3.3. Hard-core/soft-shell tunnelling representation

Accurate prediction of conductive transport near the PT requires explicit incorporation of tunnelling-mediated interactions between neighbouring conductive particles. Conventional geometric percolation approaches neglect electron transfer across nanoscale interparticle separations and therefore fail

to realistically reproduce experimentally observed conductivity evolution in conductive cementitious nanocomposites.

To address this limitation, conductive fillers were represented using a hard-core/soft-shell tunnelling formulation [20]. Within this framework, each conductive particle consists of an impenetrable hard core surrounded by an electrically active soft-shell region representing the tunnelling interaction domain. The hard core enforces geometric exclusion between conductive particles, while overlap between neighbouring soft-shell regions enables tunnelling-assisted conductive pathway formation. Figure 7 schematically illustrates the adopted hard-core/soft-shell representation.

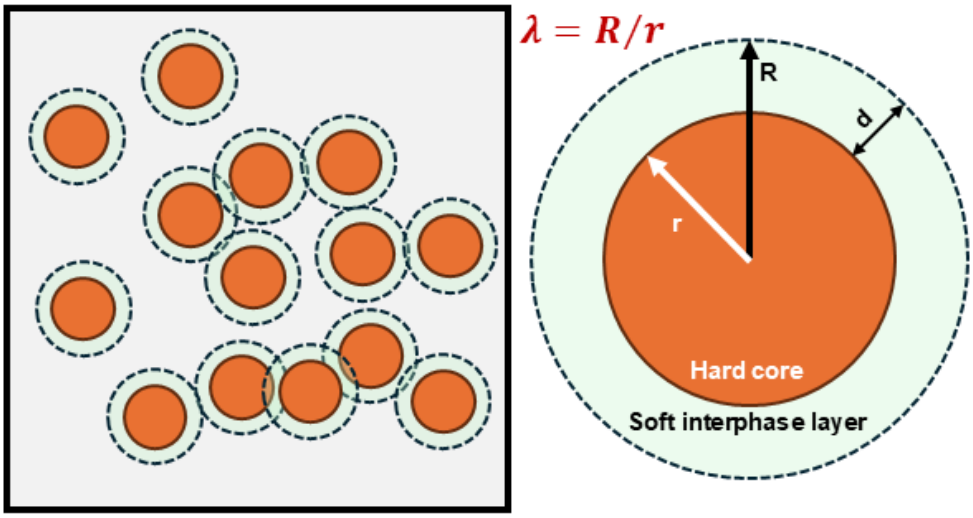

Figure 7: Conceptual hard-core/soft-shell model: Inner solid circle represents the impenetrable filler core; shaded outer region denotes the tunnelling domain.

The conductive interaction radius surrounding each conductive particle was defined using the tunnelling factor λ:

$$\lambda = \frac{R}{r} = 1 + \frac{d}{r} \tag{5}$$

where R is the total conductive interaction radius, d is the separation distance and r is the conductive particle radius. Increasing the tunnelling factor enlarges the electrically active interaction domain surrounding neighbouring conductive

particles, thereby increasing tunnelling junction density and promoting conductive pathway overlap at lower conductive filler concentrations.

The implementation of the hard-core/soft-shell model enables quantum tunnelling between adjacent CBN through overlapping interphase regions. These stages reveal the progressive development of tunnelling-mediated current pathways that bypass the need for direct particle contact, aligning with percolation theory in CBN-doped composites. The tunnelling factor serves as an effective parameter governing the spatial extent of tunnelling-assisted conductive interactions within the stochastic conductive network.

3.4. Physics-based estimation and heuristic dimensional scaling of tunnelling factor

As described by the exponential relationship in Equation (1), tunnelling conductivity decreases with increasing interparticle separation distance (d). The rate of attenuation is governed by the tunnelling decay coefficient, β, which is expressed as.

$$\beta = \frac{4\pi}{h}\sqrt{2m\phi} \tag{6}$$

where h is Planck's constant, m is the electron mass, and ϕ is the potential barrier height. A barrier height of $\phi = 1.0\,eV$ was adopted in this study, consistent with reported values for carbon-based nanomaterials embedded in a cementitious dielectric medium [47]. The effective extent of the tunnelling interphase is defined by a critical separation distance (d_{crit}), at which the tunnelling conductivity reduces to the intrinsic conductivity of the cement matrix. By equating $\sigma_{shell}(d = d_{crit})$ to the experimentally measured baseline conductivity of $2.15 \times 10^{-6}\,S/m$, the critical gap distance is obtained as $d_{crit} = 1.83\,nm$ which is consistent with values reported in the literature [48]. For a representative particle radius $r = 15\,nm$, this yields a 3D tunnelling factor:

$$\lambda_{3D} = \frac{r + d_{crit}}{r} \approx 1.12 \quad (7)$$

To apply the tunnelling parameter within the 2D RVE, a dimensional adjustment is required to account for differences in geometric connectivity between 2D and 3D systems. From a geometric perspective, the available interfacial boundary for interaction can be approximated through specific perimeter/surface scaling. In 2D, the specific perimeter of a circular particle scales as $\frac{2\pi r}{\pi r^2} = {}^{2}/_{r}$, whereas in 3D the specific surface area of a sphere scales as $\frac{4\pi r^2}{{}^{4}/_{3}\pi r^3} = {}^{3}/_{r}$, yielding a ratio of 1.5. This indicates that, at equivalent volume fractions, particles in 3D systems possess a greater interfacial area available for interaction, thereby increasing the likelihood of forming conductive pathways. This difference can be further interpreted in terms of coordination number. In idealized packing, the kissing number is 6 in 2D and 12 in 3D, indicating that a particle in 3D has approximately twice as many potential neighbouring interactions compared to 2D. The increased coordination enhances the probability of interparticle tunnelling and conductive network formation, effectively reducing the interaction range required to achieve percolation in 3D systems. In contrast, the reduced coordination in 2D limits connectivity, necessitating an enlarged effective tunnelling interaction range to reproduce comparable percolation behaviour.

Accordingly, the geometric ratio was adopted as a heuristic dimensional adjustment to estimate the effective tunnelling factor required in the 2D framework:

$$\lambda_{2D,est} = 1.5 \times \lambda_{3D} \approx 1.68 \quad (8)$$

This value provides a physically motivated reference for the subsequent parametric and statistical investigation of the tunnelling factor. It is noted that the dimensional adjustment is treated as a heuristic interpretation of the reduced connectivity of the 2D RVE rather than as a universal scaling relationship between 2D and 3D percolation systems.

4. Results

The proposed numerical framework was systematically evaluated to investigate tunnelling-mediated conductivity evolution and percolation behaviour in CBN modified cementitious composites. Particular emphasis was placed on quantifying the influence of tunnelling interaction distance and interphase conductivity evolution on conductive pathway formation, percolation sensitivity, and EEC prediction fidelity. Numerical predictions were validated against experimentally measured conductivity evolution across varying CBN concentrations using ten independent Monte Carlo realizations to ensure statistical reliability.

4.1. Conductivity evolution and percolation behaviour

Figure 8 illustrates the evolution of conductive network formation within the 2D RVEs with increasing tunnelling interaction development, i.e., the tunnelling factor λ. In the absence of tunnelling interactions (Figure 8(a)), conductive particles remain electrically isolated and the electrical potential distribution exhibits limited conductive continuity across the domain. As tunnelling-assisted conductive interactions emerge through overlapping soft-shell regions (Figure 8(b)), localized conductive pathways progressively form between neighbouring conductive particles, enabling enhanced current transport through the cementitious matrix.

With further increase in λ, conductive pathways begin to interconnect throughout the RVE domain, resulting in the formation of continuous current transport channels spanning the computational region. This transition is clearly observed in the current density distributions presented in Figure 8(c)-(e), where localized conductive regions progressively evolve into interconnected conductive networks. The formation of these continuous tunnelling-assisted conductive pathways produces the sharp conductivity increase feature of

percolation-driven conductive transport in conductive cementitious nanocomposites.

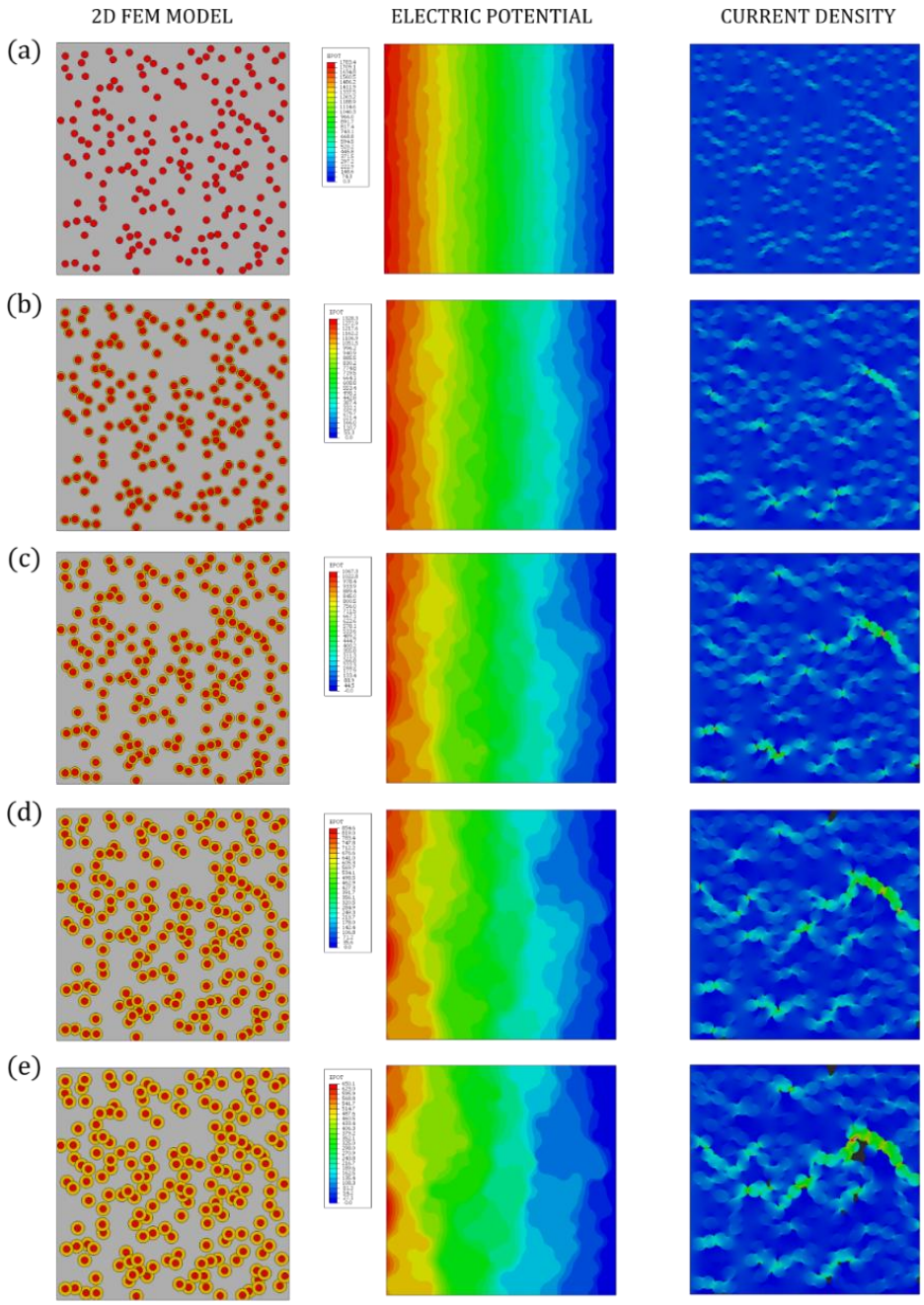

Figure 8: Evolution of tunnelling networks at 1 wt% CBN: (a) $\lambda = 1.0$: No tunnelling; (b) $\lambda = 1.4$: Incipient pathways; (c) $\lambda = 1.6$: Critical network formation; (d) $\lambda = 1.8$: Continuous conduction; (e) $\lambda = 2.0$: Continuous conduction.

Figure 9 demonstrates that the predicted conductivity evolution is strongly governed by the CBN concentrations. At low CBN concentrations, the effective electrical conductivity remains close to the matrix conductivity, whereas

increasing CBN content promotes particle contact and tunnelling-assisted connectivity. Once a continuous conductive pathway forms across the RVE, the predicted conductivity increases by several orders of magnitude, reproducing the characteristic percolation-driven transition observed experimentally between 2 and 3 wt.% CBN. This behaviour confirms that short-range tunnelling interactions play a governing role in conductive network formation in CBN modified cementitious composites.

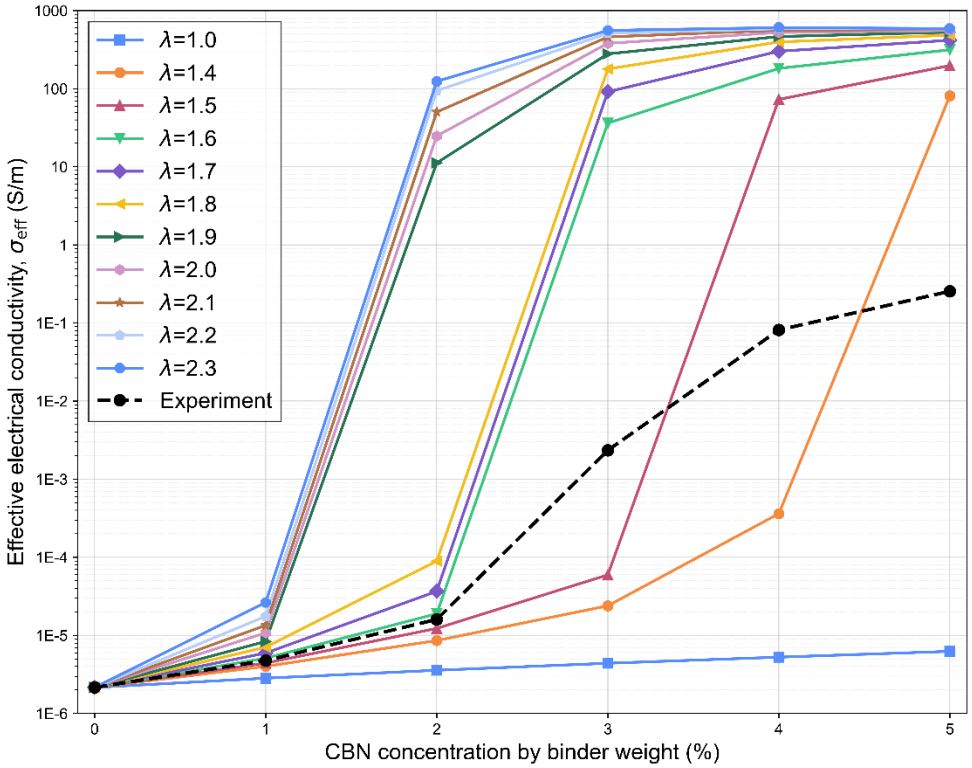

Figure 9: Predicted EEC as a function of CBN concentration for tunnelling factors ranging from λ =1.0 to 2.3, compared with the experimental measurements where the homogeneous interphase conductivity was maintained constant at $\sigma_{shell} = 277 S/m$.

4.2. Influence of tunnelling interaction distance

To investigate the influence of tunnelling-assisted conductive interactions on percolation behaviour, systematic parametric analyses were performed by varying the tunnelling factor λ from 1.0 to 2.3, while maintaining constant conductive particle radius and interphase conductivity assumptions. For this parametric study, the interphase conductivity was assumed to be equal to the intrinsic conductivity of the CBN hard core ($277\ S/m$), thereby isolating the

influence of tunnelling interaction distance on conductive network formation and conductivity evolution.

As shown in Figure 9, for $\lambda = 1.0$, corresponding to the absence of a tunnelling interaction region, the conductive particles behave as isolated hard cores and the predicted conductivity remains dominated by the cementitious matrix even at elevated conductive filler concentrations. Under these conditions, geometric particle contact alone is insufficient to produce conductive network formation within the investigated concentration range, as shown in Figure 8(a).

As the tunnelling factor increases, the electrically active interaction domain surrounding neighbouring conductive particles progressively expands, promoting conductive overlap between adjacent soft-shell regions. Consequently, localized tunnelling-assisted conductive pathways emerge at lower conductive filler concentrations, resulting in earlier conductive network formation and increased conductivity sensitivity near the PT. For tunnelling factors between approximately $\lambda = 1.6$ and $\lambda = 1.8$, the predicted conductivity evolution exhibits strong agreement with the experimentally observed conductivity transition near 2 wt.% CBN.

In particular, $\lambda = 1.7$ provides the closest agreement with experimentally measured conductivity evolution, accurately reproducing both the location of the percolation transition. Although λ was identified through comparison of numerical predictions with experimentally observed conductivity evolution, the resulting value remains physically consistent with the characteristic tunnelling interaction distance predicted by Simmons-type conductivity decay behaviour. These results demonstrate that conductive transport in CBN modified cementitious composites is highly sensitive to tunnelling interaction distance and that realistic PT prediction requires explicit incorporation of tunnelling-assisted conductive overlap mechanisms.

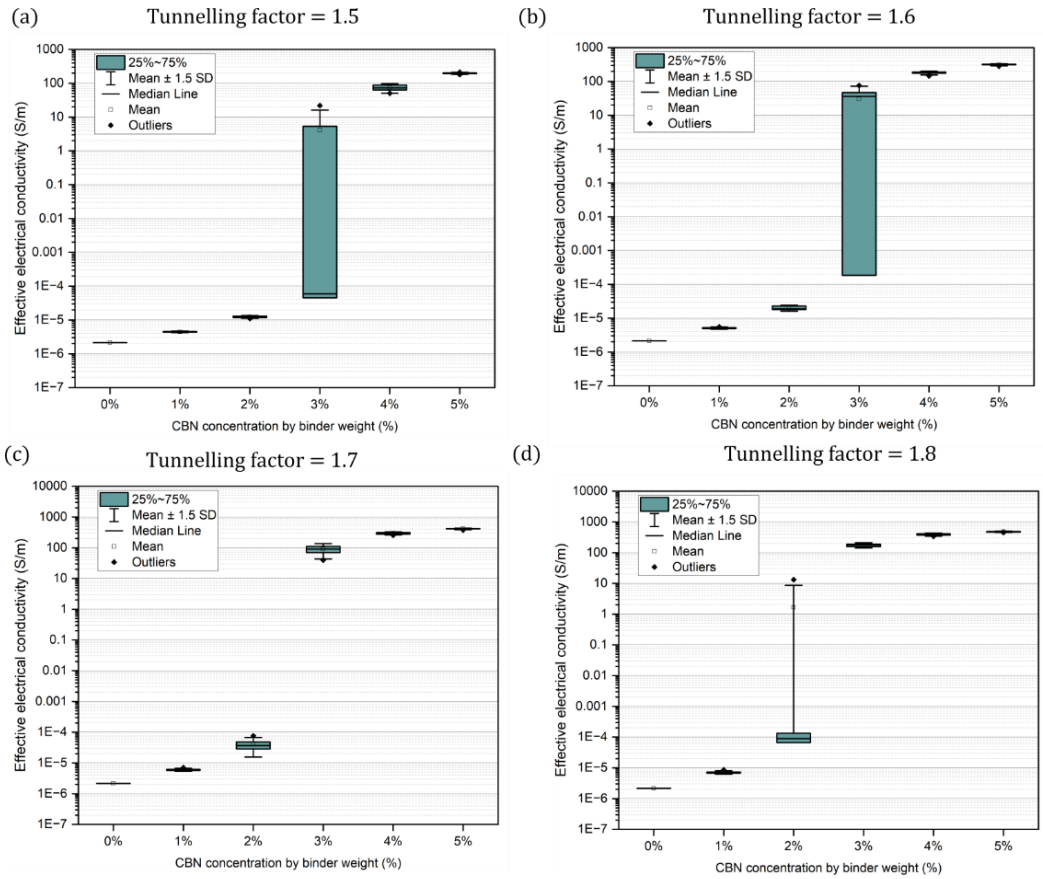

Figure 10: Statistical distribution of electrical conductivity across CBN loadings for $\lambda = 1.5$ to 1.8. Box plots represent variance across 10 trials, highlighting percolation sensitivity and optimal $\lambda = 1.7$ selection.

Figure 10 presents the statistical distribution of conductivity predictions obtained from ten independent Monte Carlo realizations for varying tunnelling factors. At lower tunnelling interaction distances, significant stochastic variability is observed due to the limited probability of conductive pathway formation within the randomly generated conductive networks. As the tunnelling factor increases, conductive overlap becomes increasingly dominant, resulting in more stable conductive connectivity and reduced variability between independent realizations.

The reduction in stochastic variability near the optimized tunnelling factor indicates that conductive transport becomes progressively governed by robust interconnected tunnelling networks rather than isolated localized conductive clusters. Consequently, the tunnelling interaction distance not only governs the

location of the PT, but also strongly influences conductive network stability and reproducibility within stochastic conductive nanocomposite systems. To assess the statistical robustness of the selected tunnelling interaction distance, an extended Monte Carlo analysis was conducted within the critical percolation transition region using 50 independent stochastic RVE realizations at 2 wt.% and 3 wt.% CBN. These concentrations were selected because both the experimental and numerical results located the percolation transition between them, where conductivity predictions are particularly sensitive to stochastic particle distribution and tunnelling-assisted connectivity. The extended analysis was used to determine whether the previously identified optimal tunnelling factor was affected by the smaller number of realizations employed in the broader parametric study. Tunnelling factors from $\lambda = 1.5$ to 1.8 were examined because conductive pathway formation within this range showed the greatest sensitivity to changes in interparticle tunnelling distance.

Figure 11 presents the mean and sample standard deviation of $\log_{10}\sigma_{eff}$ obtained from the 50 realizations. At 2 wt.% CBN, $\lambda = 1.5$, 1.6 and 1.7 maintained predominantly low-conductivity responses, indicating that stable system-spanning conductive pathways had not yet formed. For $\lambda = 1.7$, the mean logarithmic conductivity was -4.411, with a standard deviation of 0.169. In contrast, $\lambda = 1.8$ produced a substantially larger standard deviation of 1.395, indicating premature formation of high-conductivity pathways below the experimentally observed percolation threshold. At 3 wt.% CBN, $\lambda = 1.6$ exhibited a highly variable response, with a standard deviation of 2.109, reflecting the coexistence of non-percolated and percolated conductive networks. Conversely, $\lambda = 1.7$ produced a stable post-percolation response, with a mean logarithmic conductivity of 1.597 and a comparatively low standard deviation of 0.111. Although $\lambda = 1.8$ also produced stable post-percolation

conductivity at 3 wt.% CBN, its premature conductive pathway formation at 2 wt.% indicates that the corresponding tunnelling interaction distance was excessively large. These results confirm that $\lambda = 1.7$ provides the most physically representative transition from a predominantly non-percolated state at 2 wt.% CBN to stable post-percolation transport at 3 wt.% CBN. The selected value therefore provides the best balance between preventing premature conductive network formation below the experimentally observed threshold and enabling stable conductive connectivity above it.

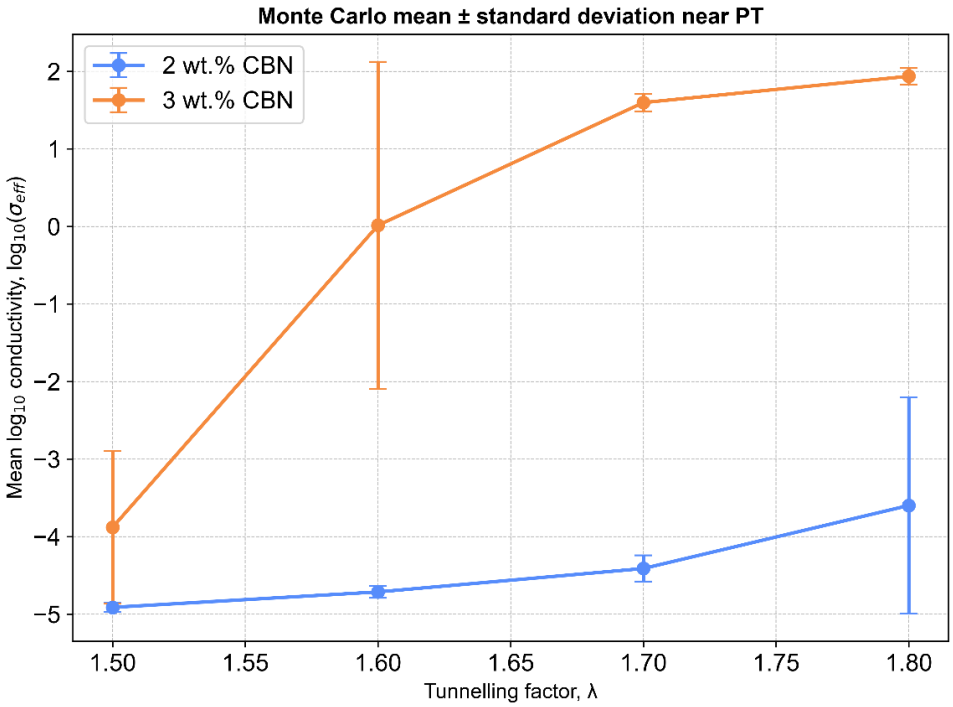

Figure 11: Mean logarithmic effective electrical conductivity and corresponding sample standard deviation obtained from 50 independent stochastic RVE realizations at 2 wt.% and 3 wt.% CBN for tunnelling factors between λ=1.5 and 1.8. The large variability observed for (λ=1.6) at 3 wt.% indicates unstable conductive network formation near the percolation boundary, whereas the large variability for (λ=1.8) at 2 wt.% indicates premature percolation. The (λ=1.7) case provides the most physically representative transition from a predominantly non-percolated state at 2 wt.% to stable post-percolation transport at 3 wt.% CBN.

A resampling assessment of the 50-realization dataset further showed that random subsets of ten realizations reproduced the full-sample mean for $\lambda = 1.7$ within 0.1 logarithmic units in 96.8% and 99.9% of cases at 2 wt.% and 3 wt.% CBN, respectively. Therefore, ten realizations were considered sufficient for identifying the relative conductivity trends and tunnelling-factor ranking in the

broader parametric study, while the extended 50-realization analysis provided additional statistical confirmation within the critical percolation transition region. The numerically selected value is also consistent with the independently derived physics-based estimate of $\lambda_{2D,est} \approx 1.68$ presented in Section 3.4. The close correspondence between the stochastic numerical selection and the Simmons-based estimate supports the physical plausibility of the adopted tunnelling interaction range. Importantly, the analytical estimate was used only to establish an expected reference range, while the final value of $\lambda = 1.7$ was selected based on the predicted percolation behaviour, experimental comparison, and statistical stability of the conductive networks. This agreement provides additional confidence that the selected tunnelling factor reflects the reduced connectivity of the 2D representation rather than serving solely as an empirically adjusted fitting parameter.

4.3. Influence of interphase conductivity evolution

It should be noted that in Section 4.2 a uniform interphase conductivity equal to the CBN conductivity is assumed. To evaluate the influence of interphase conductivity evolution on tunnelling-mediated conductive transport, systematic analyses were conducted by varying the homogeneous soft-shell interphase conductivity (σ_{shell}) between the conductivity limits of the cementitious matrix $(2.15e-6\ S/m)$ and Vulcan XC-72R® carbon black nanoparticles $(277\ S/m)$, while maintaining the optimized tunnelling factor of $\lambda = 1.7$. Figure 12 presents the predicted conductivity evolution for the investigated homogeneous interphase conductivity values.

The results demonstrate that interphase conductivity acts as a dominant governing parameter controlling conductive pathway formation and post-percolation conductivity evolution. High interphase conductivity values significantly enhance conductive overlap between neighbouring conductive

particles, resulting in earlier conductive network formation and increased EEC following the PT. Conversely, low interphase conductivity values suppress conductive connectivity and substantially underestimate experimentally observed conductivity evolution, even at elevated conductive filler concentrations.

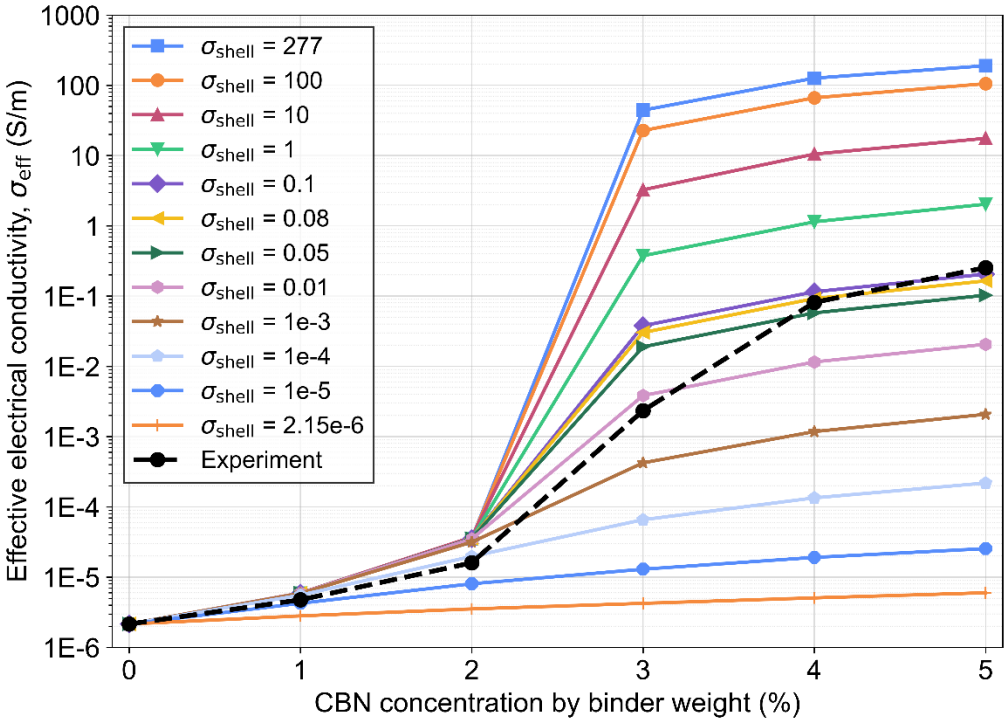

Figure 12: Influence of interphase conductivity on effective conductivity at $\lambda = 1.7$. σ_{shell} values of 0.05 to 0.1 S/m show excellent experimental correlation, validating efficient tunnelling assumptions.

Although homogeneous interphase assumptions improve conductivity prediction relative to direct-contact percolation approaches, none of the investigated homogeneous conductivity values are able to simultaneously reproduce the experimentally observed conductivity evolution across the full CBN concentration range. This limitation arises because homogeneous interphase formulations neglect the inherently distance-dependent nature of quantum tunnelling transport, where electron transfer probability decays exponentially with increasing interparticle separation distance. To address this limitation, Simmons' tunnelling formulation was incorporated through

discretized interphase conductivity modelling. The soft interphase layer is modelled using Simmon's general tunnelling equation [45] where σ_{shell} decreases exponentially with distance from the filler hard core as:

$$\sigma_{shell}(d) = \sigma_0 e^{-C_1 d} = \sigma_0 e^{-C_1(R-r)} \quad (9)$$

where $R = r + d$, r is the hard-core radius = $15\,nm$, and d is the soft interphase layer thickness, σ_0 is the filler conductivity and C_1 is the decay constant. For the selected value of $\lambda = 1.7$, the soft-interphase layer thickness (d) is calculated as $d = (\lambda - 1)r = 10.5\,nm$. At the innermost layer (immediately adjacent to the CBN core), the conductivity reaches its maximum value of $\sigma_{shell}(d = 0) = 277S/m$, corresponding to direct contact conductivity. Conversely, at the outermost layer boundary $(d = 10.5\,nm)$, conductivity decays to the matrix level of $\sigma_{shell}(d = 10.5\,nm) = 2.15e^{-6}S/m$ which yields the value of $C_1 = 1.778\,nm^{-1}$. Figure 13 illustrates the exponential decay of tunnelling conductivity with increasing radial distance from the conductive particle surface. In particular, quantum tunnelling driven conductivity exhibits the steepest gradient within the first $1.5\,nm$ from the hard-core surface, dropping from $277S/m$ to approximately $19.23S/m$ (93% reduction) over this critical distance. The results demonstrate that tunnelling conductivity decreases rapidly within the near-field interaction region surrounding the conductive particle, confirming that conductive transport is dominated by short-range tunnelling interactions.

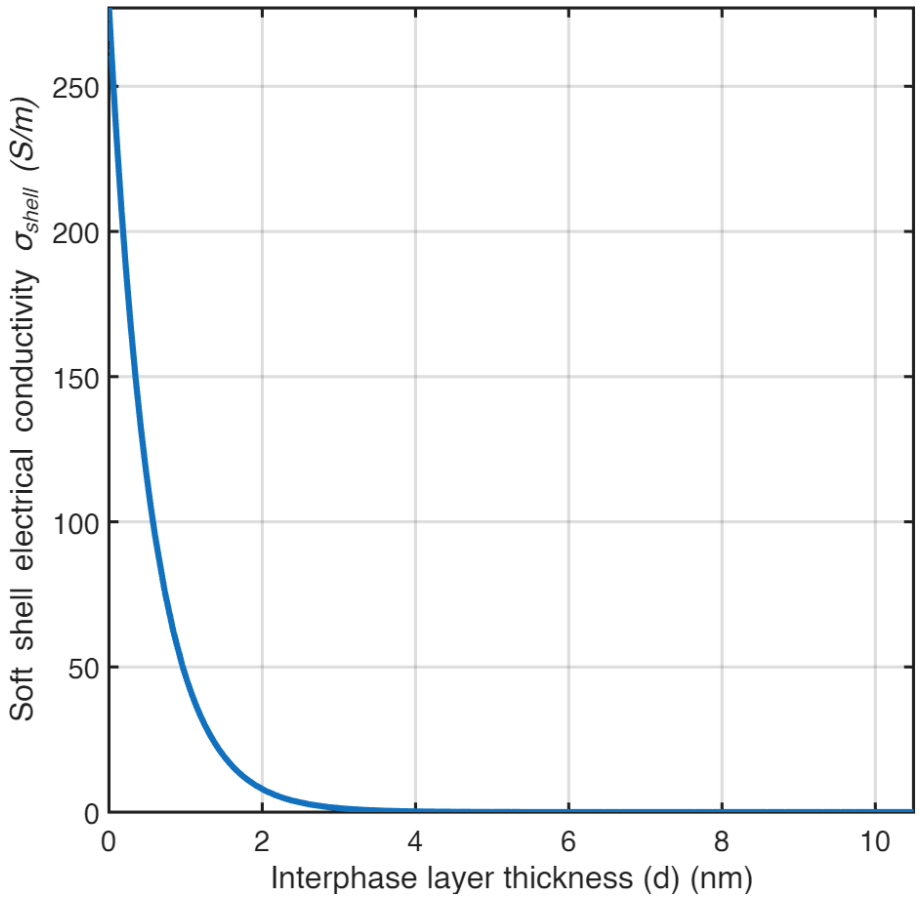

Figure 13: Exponential decay of interphase conductivity with distance from CBN surface according to Simmons' quantum tunnelling model. The rapid decay demonstrates the distance-dependent nature of quantum tunnelling, with conductivity dropping to ~7% of the maximum value at d = 1.5 nm.

To capture the steep conductivity gradients near the conductive particle surface, an adaptive layer thickness strategy with ten layers in total was further developed to be more physically appropriate as described below:

- Inner 4 layers (0 to $1.5\,nm$): $\Delta r = 0.375\,nm$ each (high resolution)
- Outer 6 layers (1.5 to $10.5\,nm$): $\Delta r = 1.5\,nm$ each (moderate resolution) as shown in Figure 14.

This graded discretization would capture 93% of the conductivity decay within the first four layers while maintaining computational efficiency.

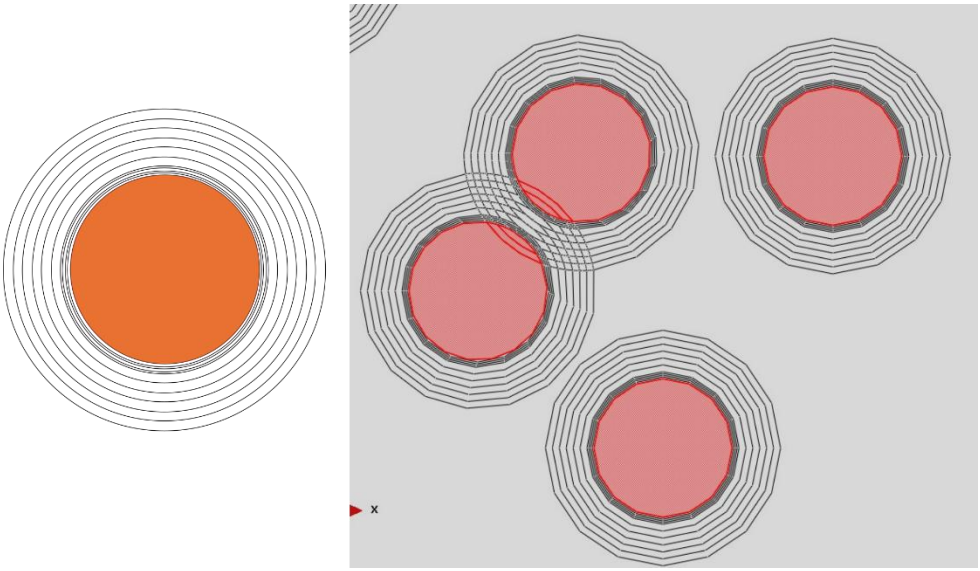

Figure 14: Ten-layer non-uniform discretization model for quantum tunnelling conductivity in CBN modified cement composites.

Higher discretization resolution was concentrated within the near-surface region where tunnelling conductivity decays most rapidly as tabulated in Table 4, while coarser discretization was employed within regions exhibiting smaller conductivity gradients.

Table 4: Layer-specific electrical conductivity values for the ten non-uniform discretized interphase regions as shown in Figure 14.

Layer reference	**Electrical conductivity** $(\sigma_{shell})\frac{S}{m}$
Layer 1 $(\sigma_{shell}(d = 0.1875\ nm))$	202.9178
Layer 2 $(\sigma_{shell}(d = 0.5625\ nm))$	108.8933
Layer 3 $(\sigma_{shell}(d = 0.9375\ nm))$	58.4361
Layer 4 $(\sigma_{shell}(d = 1.3125\ nm))$	31.359
Layer 5 $(\sigma_{shell}(d = 2.25\ nm))$	6.6155
Layer 6 $(\sigma_{shell}(d = 3.75\ nm))$	0.5486
Layer 7 $(\sigma_{shell}(d = 5.25\ nm))$	0.0455
Layer 8 $(\sigma_{shell}(d = 6.75\ nm))$	3.773e-3
Layer 9 $(\sigma_{shell}(d = 8.25\ nm))$	3.129e-4

Layer 10 $\left(\sigma_{shell}(d = 9.70\ nm)\right)$	2.595e-5

Figure 15 compares the predicted conductivity evolution obtained using the adaptive ten-layer discretization strategy with experimental measurements and previously investigated modelling approaches. The refined non-uniform discretization strategy further improves agreement with experimentally observed conductivity evolution, particularly within the immediate post-percolation regime where conductive transport is highly sensitive to localized tunnelling interactions.

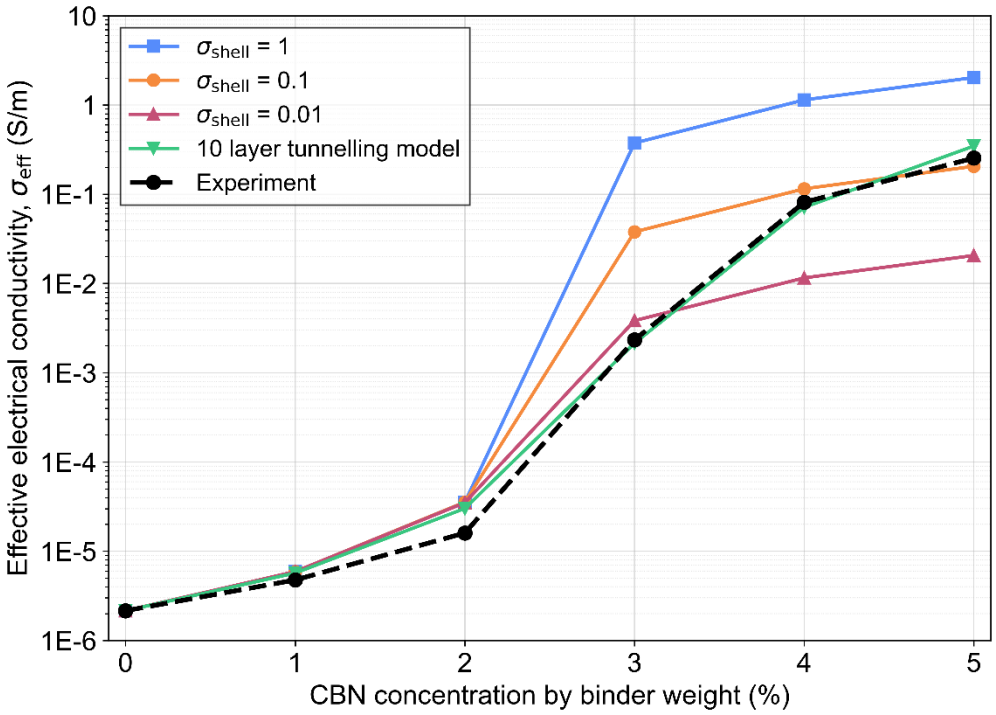

Figure 15: EEC of SSCC as a function of CBN concentration, comparing the ten-layer non-uniform discretized soft interphase model with homogeneous interphase model and experimental data.

To quantitatively evaluate the predictive capability of the proposed framework, validation analyses were subsequently conducted using relative prediction error and root mean square error (RMSE) in logarithmic conductivity space. The logarithmic formulation was adopted to account for the several-order-of-magnitude conductivity variation occurring across the percolation transition region. The RMSE was calculated as:

$$RMSE_{log} = \sqrt{\frac{1}{n}\sum_{i=1}^{n}\left(\log_{10}\sigma_i^{pred} - \log_{10}\sigma_i^{exp}\right)^2} \quad (10)$$

where σ_i^{pred} and σ_i^{exp} represent the numerically predicted and experimentally measured EEC values, respectively, and n denotes the total number of data points for comparison. The homogeneous interphase formulation yielded an RMSE value of 0.520, whereas the ten-layer discretized formulation reduced the RMSE to 0.132. This corresponds to an approximate 75% reduction in logarithmic conductivity prediction error for the ten-layer discretized framework relative to the homogeneous interphase model. The results demonstrate that explicit incorporation of distance-dependent tunnelling conductivity evolution is essential for physically realistic prediction of conductive transport and percolation behaviour in conductive cementitious nanocomposites.

4.4. Computational efficiency and modelling implications

Compared with the homogeneous single-layer interphase formulation, the adaptive ten-layer discretized framework required substantially greater computational effort. For example, for a 2D RVE containing 4 wt.% CBN (545 particles within a 1000 nm × 1000 nm domain), the homogeneous soft-shell model required approximately 40 seconds for model generation and 57 seconds for simulation. In comparison, the adaptive ten-layer formulation required approximately 2.5 hours for model generation and an additional 15 minutes for simulation, mainly from the rapid increase in geometric partitions, interphase interactions, and conductive domain discretization associated with multilayer tunnelling representations.

Despite the increased computational demand associated with multilayer tunnelling discretization, the proposed 2D multiscale framework remains computationally tractable relative to fully resolved 3D multilayer conductive network simulations. More importantly, the framework successfully reproduces

the experimentally observed conductivity transition and percolation behaviour while explicitly incorporating distance-dependent tunnelling conductivity evolution. The results further demonstrate that physically realistic prediction of conductive transport in low-aspect-ratio conductive filler systems cannot be achieved using purely geometric percolation approaches or homogeneous interphase assumptions alone. Instead, accurate prediction of conductive pathway evolution and percolation sensitivity requires explicit incorporation of spatially varying tunnelling conductivity within the electrically active interphase domain.

5. Conclusions

This study developed a physics-informed multiscale numerical framework for predicting tunnelling-mediated conductivity evolution and percolation behaviour in carbon black nanoparticle modified cementitious composites. The proposed framework combines stochastic representative volume element generation, electro-thermal finite element simulation, and distance-dependent tunnelling conductivity modelling to capture conductive pathway formation within heterogeneous cementitious microstructures.

The main conclusions are:

- The experimentally measured conductivity evolution exhibited a pronounced percolation transition between 2 and 3 wt.% CBN, where EEC increased by several orders of magnitude. This transition confirms the formation of interconnected conductive pathways within the cementitious matrix.
- The hard-core/soft-shell tunnelling formulation demonstrated that conductive network formation in low-aspect-ratio carbon black systems cannot be explained by direct particle contact alone. Instead, tunnelling-assisted interactions between neighbouring particles play a governing role in percolation development.
- The tunnelling interaction distance governed both percolation behaviour and conductive network stability. The selected factor, $\lambda = 1.7$, reproduced the

experimental conductivity transition, reduced stochastic variability near percolation, and closely matched the physics-based estimate of 1.68, confirming that it reflects the reduced connectivity of the 2D RVE rather than serving solely as a fitted parameter.

- Homogeneous interphase conductivity assumptions were insufficient to accurately reproduce the sharp conductivity transition observed experimentally. This limitation arises from the inability of homogeneous interphase models to represent the exponential distance dependence of quantum tunnelling conductivity.
- The ten-layer discretized tunnelling formulations significantly improved prediction accuracy by incorporating Simmons-type exponential conductivity decay within the electrically active interphase region, reducing the logarithmic RMSE from 0.520 for the homogeneous model to 0.132.

Overall, the findings demonstrate that distance-dependent tunnelling conductivity is essential for physically realistic prediction of percolation-driven conductivity evolution in carbon black cementitious composites. By explicitly incorporating tunnelling-mediated transport, the framework offers a scalable numerical tool for optimizing conductive filler dosage in self-sensing cementitious materials, providing a foundation for future extension toward strain-dependent piezoresistive modelling and electromechanical self-sensing performance prediction.

Despite the strong predictive capability of the proposed framework, several limitations remain that warrant further investigation. The current model assumes isotropic and monodisperse CBNs, which simplifies conductive network generation but may not fully capture the effects of particle agglomeration, irregular morphology, and size variability commonly observed in practical cementitious nanocomposites. Furthermore, the present framework does not explicitly incorporate microstructural defects such as pores, voids, and microcracks, which can significantly influence conductive pathway continuity, EEC, and percolation behaviour by introducing localized resistive barriers within the conductive network. Finally, the adopted 2D RVE framework, while computationally efficient,

additionally simplifies the 3D conductive connectivity present in realistic cementitious systems, where conductive pathway formation is expected to occur at shorter average tunnelling distances, thereby reducing the effective tunnelling interaction factor required for conductive percolation relative to equivalent 2D systems.

Author Contributions

Jeslin Thalapil: Conceptualization, Methodology, Investigation, Software, Validation, Visualization, Writing - Original Draft.

Ye Lu: Conceptualization, Methodology, Investigation, Resources, Supervision, Writing - Original Draft, Writing - Review & Editing.

Data availability statement

The data that support the findings of this study are available from the corresponding author upon reasonable request

Funding statement

The author(s) received no financial support for the research, authorship, and/or publication of this article.

Conflicts of Interest

The authors declare that they have no known competing financial interests or personal relationships that could have appeared to influence the work reported in this paper.

References

[1] P.J.M. Monteiro, S.A. Miller, A. Horvath, Towards sustainable concrete, Nat. Mater. 16 (2017) 698–699. https://doi.org/10.1038/nmat4930.

[2] P.K. Mehta, Concrete: microstructure, properties, and materials, 4th ed, McGraw-Hill, New York, 2014.

[3] A.M. Neville, Properties of concrete, Ed. 5th, Pearson, Noida, 2013.

[4] V.R. Gharehbaghi, E. Noroozinejad Farsangi, M. Noori, T.Y. Yang, S. Li, A. Nguyen, C. Málaga-Chuquitaype, P. Gardoni, S. Mirjalili, A Critical Review on Structural Health Monitoring: Definitions, Methods, and Perspectives, Arch. Comput. Methods Eng. 29 (2022) 2209–2235. https://doi.org/10.1007/s11831-021-09665-9.

[5] C.R. Farrar, K. Worden, Structural health monitoring: a machine learning perspective, Wiley, Chichester, West Sussex, U.K. ; Hoboken, N.J, 2013.

[6] J.P. Lynch, A Summary Review of Wireless Sensors and Sensor Networks for Structural Health Monitoring, Shock Vib. Dig. 38 (2006) 91–128. https://doi.org/10.1177/0583102406061499.

[7] A. Dinesh, S. Indhumathi, M. Pichumani, Self-sensing cement composites for structural health monitoring: From know-how to do-how, Autom. Constr. 160 (2024) 105304. https://doi.org/10.1016/j.autcon.2024.105304.

[8] D.D.L. Chung, Carbon materials for structural self-sensing, electromagnetic shielding and thermal interfacing, Carbon 50 (2012) 3342–3353. https://doi.org/10.1016/j.carbon.2012.01.031.

[9] B. Han, S. Ding, X. Yu, Intrinsic self-sensing concrete and structures: A review, Measurement 59 (2015) 110–128. https://doi.org/10.1016/j.measurement.2014.09.048.

[10] S. Wen, D.D.L. Chung, Partial replacement of carbon fiber by carbon black in multifunctional cement–matrix composites, Carbon 45 (2007) 505–513. https://doi.org/10.1016/j.carbon.2006.10.024.
[11] J. Han, J. Pan, J. Cai, X. Li, A review on carbon-based self-sensing cementitious composites, Constr. Build. Mater. 265 (2020) 120764. https://doi.org/10.1016/j.conbuildmat.2020.120764.
[12] Y. Wang, Y. Wang, B. Wan, B. Han, G. Cai, Z. Li, Properties and mechanisms of self-sensing carbon nanofibers/epoxy composites for structural health monitoring, Compos. Struct. 200 (2018) 669–678. https://doi.org/10.1016/j.compstruct.2018.05.151.
[13] X. Jiang, D. Lu, B. Yin, Z. Leng, Advancing carbon nanomaterials-engineered self-sensing cement composites for structural health monitoring: A state-of-the-art review, J. Build. Eng. 87 (2024) 109129. https://doi.org/10.1016/j.jobe.2024.109129.
[14] A. Al-Dahawi, M.H. Sarwary, O. Öztürk, G. Yıldırım, A. Akın, M. Şahmaran, M. Lachemi, Electrical percolation threshold of cementitious composites possessing self-sensing functionality incorporating different carbon-based materials, Smart Mater. Struct. 25 (2016) 105005. https://doi.org/10.1088/0964-1726/25/10/105005.
[15] D.D.L. Chung, Carbon materials for structural self-sensing, electromagnetic shielding and thermal interfacing, Carbon 50 (2012) 3342–3353. https://doi.org/10.1016/j.carbon.2012.01.031.
[16] F. Azhari, N. Banthia, Cement-based sensors with carbon fibers and carbon nanotubes for piezoresistive sensing, Cem. Concr. Compos. 34 (2012) 866–873. https://doi.org/10.1016/j.cemconcomp.2012.04.007.
[17] G.H. Nalon, J.C.L. Ribeiro, E.N.D.D. Araújo, L.G. Pedroti, J.M.F.D. Carvalho, R.F. Santos, A. Aparecido-Ferreira, Effects of different kinds of carbon black nanoparticles on the piezoresistive and mechanical properties of cement-based composites, J. Build. Eng. 32 (2020) 101724. https://doi.org/10.1016/j.jobe.2020.101724.
[18] M.S. Qasim, F. Shabbir, Q.U.Z. Khan, A. Raza, Investigation on Self-Sensing Capability of Different Grades of Carbon Black in Cementitious Composites, Iran. J. Sci. Technol. Trans. Civ. Eng. 47 (2023) 761–774. https://doi.org/10.1007/s40996-022-00890-1.
[19] A. D'Alessandro, M. Rallini, F. Ubertini, A.L. Materazzi, J.M. Kenny, Investigations on scalable fabrication procedures for self-sensing carbon nanotube cement-matrix composites for SHM applications, Cem. Concr. Compos. 65 (2016) 200–213. https://doi.org/10.1016/j.cemconcomp.2015.11.001.
[20] L. Berhan, A.M. Sastry, Modeling percolation in high-aspect-ratio fiber systems. I. Soft-core versus hard-core models, Phys. Rev. E 75 (2007) 041120. https://doi.org/10.1103/PhysRevE.75.041120.
[21] H. Jung, H.K. Choi, J. Yu, Prediction and experimental validation of composite strength by applying modified micromechanics for composites containing multiple distinct heterogeneities, Compos. Part B Eng. 91 (2016) 1–7. https://doi.org/10.1016/j.compositesb.2015.12.043.
[22] Z. Liu, W. Peng, Y. Zare, D. Hui, K.Y. Rhee, Predicting the electrical conductivity in polymer carbon nanotube nanocomposites based on the volume fractions and resistances of the nanoparticle, interphase, and tunneling regions in conductive networks, RSC Adv. 8 (2018) 19001–19010. https://doi.org/10.1039/C8RA00811F.
[23] Y. Zare, K.Y. Rhee, A power model to predict the electrical conductivity of CNT reinforced nanocomposites by considering interphase, networks and tunneling condition, Compos. Part B Eng. 155 (2018) 11–18.
[24] S.Y. Kim, Y.J. Noh, J. Yu, Prediction and experimental validation of electrical percolation by applying a modified micromechanics model considering multiple heterogeneous inclusions, Compos. Sci. Technol. 106 (2015) 156–162. https://doi.org/10.1016/j.compscitech.2014.11.015.

[25] D.S. McLachlan, M. Blaszkiewicz, R.E. Newnham, Electrical Resistivity of Composites, J. Am. Ceram. Soc. 73 (1990) 2187–2203. https://doi.org/10.1111/j.1151-2916.1990.tb07576.x.
[26] Y. Zare, K.Y. Rhee, Simplification and development of McLachlan model for electrical conductivity of polymer carbon nanotubes nanocomposites assuming the networking of interphase regions, Compos. Part B Eng. 156 (2019) 64–71.
[27] X. Lu, J. Yvonnet, F. Detrez, J. Bai, Low electrical percolation thresholds and nonlinear effects in graphene-reinforced nanocomposites: A numerical analysis, J. Compos. Mater. 52 (2018) 2767–2775. https://doi.org/10.1177/0021998317753888.
[28] J. Bartels, E. Kuhn, J.-P. Jürgens, V. Ploshikhin, Mesoscopic simulation of the electrical conductivity of carbon nanotube reinforced polymers regarding atomistic results, J. Compos. Mater. 52 (2018) 331–339. https://doi.org/10.1177/0021998317706537.
[29] W. Song, V. Krishnaswamy, R.V. Pucha, Computational homogenization in RVE models with material periodic conditions for CNT polymer composites, Compos. Struct. 137 (2016) 9–17. https://doi.org/10.1016/j.compstruct.2015.11.013.
[30] G.P. Moriarty, J.H. Whittemore, K.A. Sun, J.W. Rawlins, J.C. Grunlan, Influence of polymer particle size on the percolation threshold of electrically conductive latex-based composites, J. Polym. Sci. Part B Polym. Phys. 49 (2011) 1547–1554.
[31] G. Wang, C. Wang, C. Tang, F. Zhang, T. Sun, X. Yu, Two-stage electrical percolation of metal nanoparticle–polymer nanocomposites, J. Phys. Chem. C 122 (2018) 8614–8620.
[32] S. Nayak, S. Das, A microstructure-guided numerical approach to evaluate strain sensing and damage detection ability of random heterogeneous self-sensing structural materials, Comput. Mater. Sci. 156 (2019) 195–205. https://doi.org/10.1016/j.commatsci.2018.09.035.
[33] D.-W. Kim, J.H. Lim, J. Yu, Efficient prediction of the electrical conductivity and percolation threshold of nanocomposite containing spherical particles with three-dimensional random representative volume elements by random filler removal, Compos. Part B Eng. 168 (2019) 387–397. https://doi.org/10.1016/j.compositesb.2019.03.038.
[34] Z. Shi, T.T. Nguyen, H.H. Bui, Y. Lu, Discrete element modelling of electro-mechanical behaviour in modified cementitious materials, Int. J. Mech. Sci. 291–292 (2025) 110152. https://doi.org/10.1016/j.ijmecsci.2025.110152.
[35] S. Pérez-Rodríguez, E. Pastor, M.J. Lázaro, Electrochemical behavior of the carbon black Vulcan XC-72R: Influence of the surface chemistry, Int. J. Hydrog. Energy 43 (2018) 7911–7922. https://doi.org/10.1016/j.ijhydene.2018.03.040.
[36] S. Khodabakhshi, P.F. Fulvio, E. Andreoli, Carbon black reborn: Structure and chemistry for renewable energy harnessing, Carbon 162 (2020) 604–649. https://doi.org/10.1016/j.carbon.2020.02.058.
[37] T.D. Vu, S. Gwon, Y.C. Choi, M. Shin, Self-heating performance of cement composites devised with carbon black and carbon fiber: Roles of superplasticizer and silica fume, J. Build. Eng. 80 (2023) 108054. https://doi.org/10.1016/j.jobe.2023.108054.
[38] H. Dehghanpour, K. Yilmaz, M. Ipek, Evaluation of recycled nano carbon black and waste erosion wires in electrically conductive concretes, Constr. Build. Mater. 221 (2019) 109–121. https://doi.org/10.1016/j.conbuildmat.2019.06.025.
[39] A. Naqi, N. Abbas, N. Zahra, A. Hussain, S.Q. Shabbir, Effect of multi-walled carbon nanotubes (MWCNTs) on the strength development of cementitious materials, J. Mater. Res. Technol. 8 (2019) 1203–1211. https://doi.org/10.1016/j.jmrt.2018.09.006.
[40] W. Dong, W. Li, Y. Guo, X. He, D. Sheng, Effects of silica fume on physicochemical properties and piezoresistivity of intelligent carbon black-cementitious composites, Constr. Build. Mater. 259 (2020) 120399. https://doi.org/10.1016/j.conbuildmat.2020.120399.

[41] G.M. Kim, I.W. Nam, B. Yang, H.N. Yoon, H.K. Lee, S. Park, Carbon nanotube (CNT) incorporated cementitious composites for functional construction materials: The state of the art, Compos. Struct. 227 (2019) 111244. https://doi.org/10.1016/j.compstruct.2019.111244.
[42] Z. Shi, L. Hua, Y. Lu, D. Shen, D. Huang, Investigation of carbon black nanoparticle modified cementitious composites for sensing dynamic vibro-acousto signals, Measurement 237 (2024) 115231. https://doi.org/https://doi.org/10.1016/j.measurement.2024.115231.
[43] D.D.L. Chung, A critical review of electrical-resistance-based self-sensing in conductive cement-based materials, Carbon 203 (2023) 311–325. https://doi.org/10.1016/j.carbon.2022.11.076.
[44] Z. Shi, L. Hua, Y. Lu, D. Shen, D. Huang, Investigation of carbon black nanoparticle modified cementitious composites for sensing dynamic vibro-acousto signals, Measurement 237 (2024) 115231. https://doi.org/10.1016/j.measurement.2024.115231.
[45] J.G. Simmons, Generalized Formula for the Electric Tunnel Effect between Similar Electrodes Separated by a Thin Insulating Film, J. Appl. Phys. 34 (1963) 1793–1803. https://doi.org/10.1063/1.1702682.
[46] S. Pérez-Rodríguez, E. Pastor, M.J. Lázaro, Electrochemical behavior of the carbon black Vulcan XC-72R: Influence of the surface chemistry, Int. J. Hydrog. Energy 43 (2018) 7911–7922. https://doi.org/10.1016/j.ijhydene.2018.03.040.
[47] M. Saberi, A. Moradi, R. Ansari, M.K. Hassanzadeh-Aghdam, J. Jamali, Developing an efficient analytical model for predicting the electrical conductivity of polymeric nanocomposites containing hybrid carbon nanotube/carbon black nanofillers, Compos. Part Appl. Sci. Manuf. 185 (2024) 108374. https://doi.org/10.1016/j.compositesa.2024.108374.
[48] M. Mazaheri, J. Payandehpeyman, S. Jamasb, Modeling of Effective Electrical Conductivity and Percolation Behavior in Conductive-Polymer Nanocomposites Reinforced with Spherical Carbon Black, Appl. Compos. Mater. 29 (2022) 695–710. https://doi.org/10.1007/s10443-021-09991-y.